Research Square

Preprints are preliminary reports that have not undergone peer review.
They should not be considered conclusive, used to inform clinical practice,
or referenced by the media as validated information.

Dielectric and electrical properties of sol-gel γ-Fe2O3 nanoparticles: polaron hopping and a thermal crossover of the transport regime

L. Chouiref
Gabes University
I. Najeh
Imededdine.Najeh@gmail.com

Gabes University
O. M. Lemine
Imam Mohammad Ibn Saud Islamic University (IMISU)
L. El Mir
Gabes University

Research Article

Keywords: γ-Fe2O3; sol-gel method; small polarons; impedance spectroscopy; electric modulus; Jonscher power law; dielectric relaxation; electrical conductivity; Fe2+ carrier generation

Posted Date: November 12th, 2026

DOI: https://doi.org/10.21203/rs.3.rs-11487955/v1

License: This work is licensed under a Creative Commons Attribution 4.0 International License.
Read Full License

Additional Declarations: No competing interests reported.

Dielectric and electrical properties of sol-gel γ-Fe_2O_3 nanoparticles: polaron hopping and a thermal crossover of the transport regime

L. Chouiref[1], I. Najeh[1,*], O. M. Lemine [2], L. El Mir[1]

[1] Laboratory of Physics of Materials and Nanomaterials Applied at Environment (LaPhyMNE), Faculty of Sciences in Gabes, Gabes University, 6072 Gabes, Tunisia.

[2] Department of Physics, College of Sciences, Imam Mohammad Ibn Saud Islamic University (IMISU), Riyadh 11623, Saudi Arabia.

* Corresponding author: Dr Najeh Imededdine Imededdine.Najeh@gmail.com

Abstract

γ-Fe_2O_3 nanoparticles prepared by the sol-gel method (supercritical drying in ethanol) were characterized by XRD, TEM/HRTEM and Raman spectroscopy, which indicate a single-phase cubic spinel structure (maghemite-like) made of quasi-spherical, essentially single-crystalline nanoparticles (crystallite size of about 9–12 nm from XRD; mean TEM diameter of about 7 nm). Their electrical and dielectric properties were studied by impedance spectroscopy between 300 and 600 K. Below ≈ 420 K the ac conductivity is dispersive and follows Jonscher's power law, with a frequency exponent s that varies non-monotonically with temperature (minimum near 340 K); above ≈ 440 K it is frequency independent. The thermally activated conductivity, the low activation energies at low temperature (100–300 meV from the ac data; 315 meV from the impedance fits) and the behavior of s(T) are consistent with charge transport by hopping of small polarons between Fe^{2+} and Fe^{3+} ions, with a probable crossover from correlated-barrier-hopping/overlapping-large-polaron to non-overlapping small-polaron tunneling; Mott's variable-range hopping is ruled out. The Fe^{2+} carriers are attributed to the reducing synthesis medium and to the oxygen-deficient surface of the ~7 nm particles, and the hopping barrier to the reorganization energy of the Fe^{2+}/Fe^{3+} electron transfer. The activation energy increases to 0.73 eV above 440 K and the conductivity rises about sevenfold between 420 and 440 K, whereas an Arrhenius extrapolation predicts only ≈ 2.5; we tentatively interpret this step as the thermally activated release of additional Fe^{2+} carriers (loss of surface hydroxyl groups and oxygen) combined with the activation of the inter-particle contacts of the aerogel network, which carry the long-range current.

Keywords. γ-Fe_2O_3; sol-gel method; small polarons; impedance spectroscopy; electric modulus; Jonscher power law; dielectric relaxation; electrical conductivity; Fe^{2+} carrier generation.

1. Introduction

Maghemite (γ-Fe_2O_3) is a ferrimagnetic iron oxide with an inverse-spinel structure containing cation vacancies, and it has attracted sustained interest because of its magnetic properties [1–3]. In nanoparticle form it is superparamagnetic at room temperature below the single-domain size [4].

Ferrites are widely used in electronics (filters, transformer cores and other components) because of their electrical characteristics [1–3], although their performance in applications depends first on their magnetic behavior [5,6]. The properties of iron oxide nanoparticles are strongly influenced by the synthesis route and conditions, such as the chemical method and the synthesis temperature [7].

The electrical transport and the dielectric relaxation of maghemite nanoparticles remain much less documented than their magnetic properties, and the nature of the charge carriers and of the hopping mechanism is still debated. Recent studies show that conduction in Fe_3O_4 nanoparticles is governed by polaron hopping between Fe^{2+} and Fe^{3+} ions, with a smooth crossover from correlated barrier hopping to non-overlapping small-polaron tunneling and a Verwey transition that is often suppressed at the nanoscale, while γ-Fe_2O_3 shows Jonscher-type ac conductivity, low dielectric loss, and non-Debye relaxation dominated by grain boundaries and Maxwell–Wagner interfacial polarization.

In this work, we study the structural, electrical (ac and dc conductivity, impedance, electric modulus) and dielectric properties of γ-Fe_2O_3 nanoparticles prepared by the sol-gel method between 300 and 600 K, in order to identify the conduction mechanism and the role of the contacts between nanoparticles. A sharp change of the conduction regime near 430 K is reported and tentatively interpreted in terms of thermally activated Fe^{2+} carrier generation and activation of the inter-particle contacts. The uses of the nanoparticles that follow directly from these results (temperature sensing, dielectric and electronic components, and potential biomedical applications of the superparamagnetic nanoparticles) are indicated in the discussion and in the conclusion.

2. Materials and method

Maghemite nanoparticles were prepared by a sol–gel route followed by supercritical drying in ethanol, as detailed in our earlier studies [8,9]. The preparation, illustrated in Fig. 1, starts

from iron(III) acetylacetonate, $Fe(C_5H_7O_2)_3$, which is the only iron source. A solution of 16 g of this precursor in 32 mL of ethanol was kept under magnetic stirring for 10 min. In the Gd-doped variants of this protocol, gadolinium acetate dihydrate is introduced at this stage; no dopant was added in the present work. After a further 15 min of stirring, the mixture was diluted with 220 mL of ethanol and sealed in an autoclave, where the solvent was brought above its critical point (T_c = 243 °C, P_c = 63.6 bar) and removed under these supercritical conditions, leaving a dry, brown aerogel powder. This procedure is simple and cost-effective, and it can be scaled up to produce large quantities of γ-Fe_2O_3 nanoparticles.

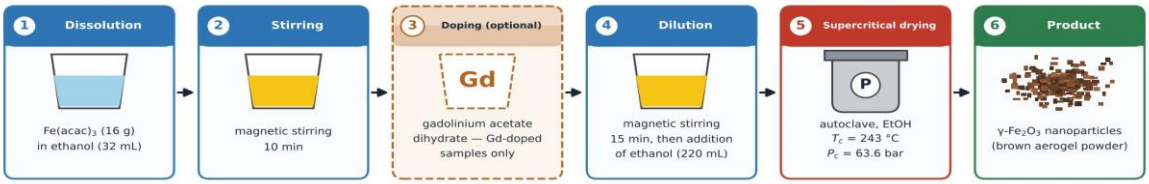


Fig. 1. Flow diagram of the modified sol–gel synthesis (supercritical drying in ethanol) of γ-Fe_2O_3 nanoparticles. Step 3 (dashed) applies only to Gd-doped samples and was not used in this work.

In this approach [7,9], the water needed for hydrolysis is released slowly through an esterification reaction, which allows the size of the growing nanoparticles to be controlled, and the supercritical drying preserves the open network of the gel, which explains the loosely connected, aerogel-like arrangement of the particles observed by TEM.

The crystal structure was examined by X-ray diffraction (XRD) using a Bruker D8 Advance diffractometer (40 kV, 30 mA) with Co Kα radiation (λ = 1.78901 Å). Data were collected over 2θ = 20–70° with a step size of 0.02°. The average crystallite size, D, was estimated from the Scherrer formula [10], $D = \frac{K\lambda}{B\cos\theta}$, where K ≈ 0.9 is the shape factor, λ is the X-ray wavelength, θ is the Bragg angle, and B is the full width at half maximum (FWHM) of the diffraction peak, in radians. The morphology, size distribution and chemical composition of the particles were investigated using a Nova NanoSEM 200 field-emission scanning electron microscope (FE-SEM) coupled with energy-dispersive X-ray spectroscopy (EDAX), and a JEOL transmission electron microscope (TEM). Impedance spectra were recorded between 100 Hz and 1 MHz from 300 to 600 K in steps of 20 K.

3. Results and discussion

The elemental composition of the powders was checked by energy-dispersive X-ray (EDX/EDAX) analysis, and the spectrum is shown in Fig. 2. It contains only the lines of iron (Fe Kα and Kβ at ≈ 6.4 and 7.1 keV, Fe L at low energy) and of oxygen (O Kα, below 1 keV);

no other element is detected within the sensitivity of the technique, which supports the chemical purity of the iron oxide. The quantification gives 72.8 ± 0.2 wt% Fe and 27.2 ± 0.2 wt% O, i.e. an O/Fe atomic ratio of ≈ 1.30. This value is lower than that of stoichiometric γ-Fe_2O_3 (O/Fe = 1.5; 69.9 wt% Fe) and close to that of Fe_3O_4 (O/Fe = 1.33; 72.4 wt% Fe), which would point to an oxygen-deficient, partially reduced oxide. This result must nevertheless be regarded as semi-quantitative, because the O Kα line is low in energy and strongly absorbed, and because standardless EDX is less accurate for light elements. Moreover, a ratio below that of Fe_3O_4 would imply an oxide more reduced than magnetite, which is not supported by the XRD, Raman and lattice-parameter results discussed below: the oxygen content is most probably underestimated, and this ratio cannot be used as a measure of the Fe^{2+} content.

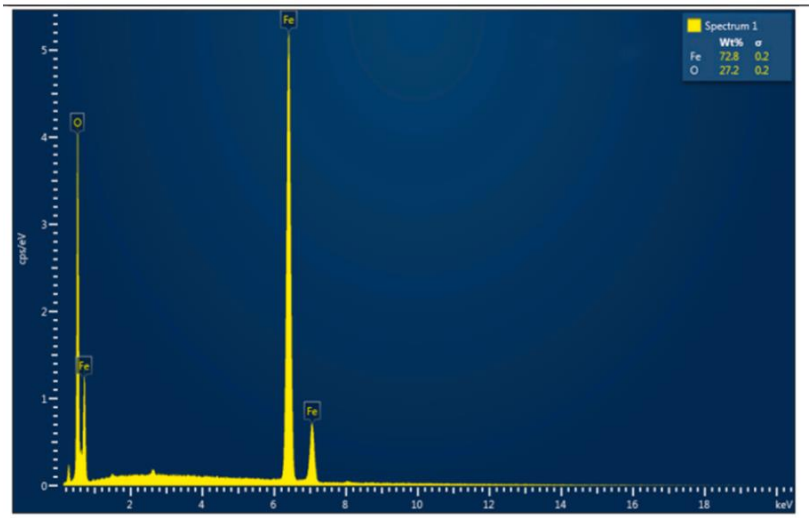


Fig. 2. Energy-dispersive X-ray (EDX) spectrum of the sol–gel iron oxide nanopowder

The TEM image of the γ-Fe_2O_3 (Fig. 3c) shows quasi-spherical nanoparticles grouped in loosely connected clusters, as expected for an aerogel network. The particle-size distribution (Fig. 3d), obtained by measuring N = 55 particles on the TEM micrographs, extends from 2 to 14 nm, with a mean diameter ⟨D⟩ = 7.2 nm, a standard deviation σ = 2.2 nm (σ/⟨D⟩ ≈ 30 %) and a mode at 7–8 nm. This number-weighted mean is smaller than the volume-weighted crystallite size deduced from the XRD analysis (≈ 12 nm, see below). For a distribution of this width (σ/⟨D⟩ ≈ 0.3) the volume-weighted mean diameter $\langle D^4\rangle/\langle D^3\rangle$ is expected to be about 8.9 nm (assuming a normal distribution and spherical particles), i.e. roughly 25 % larger than the number-weighted mean (Fig. 3d); the larger value obtained from the Williamson–Hall analysis is discussed below. The crystal structure of the nanoparticles is represented in Fig. 3f and described below.

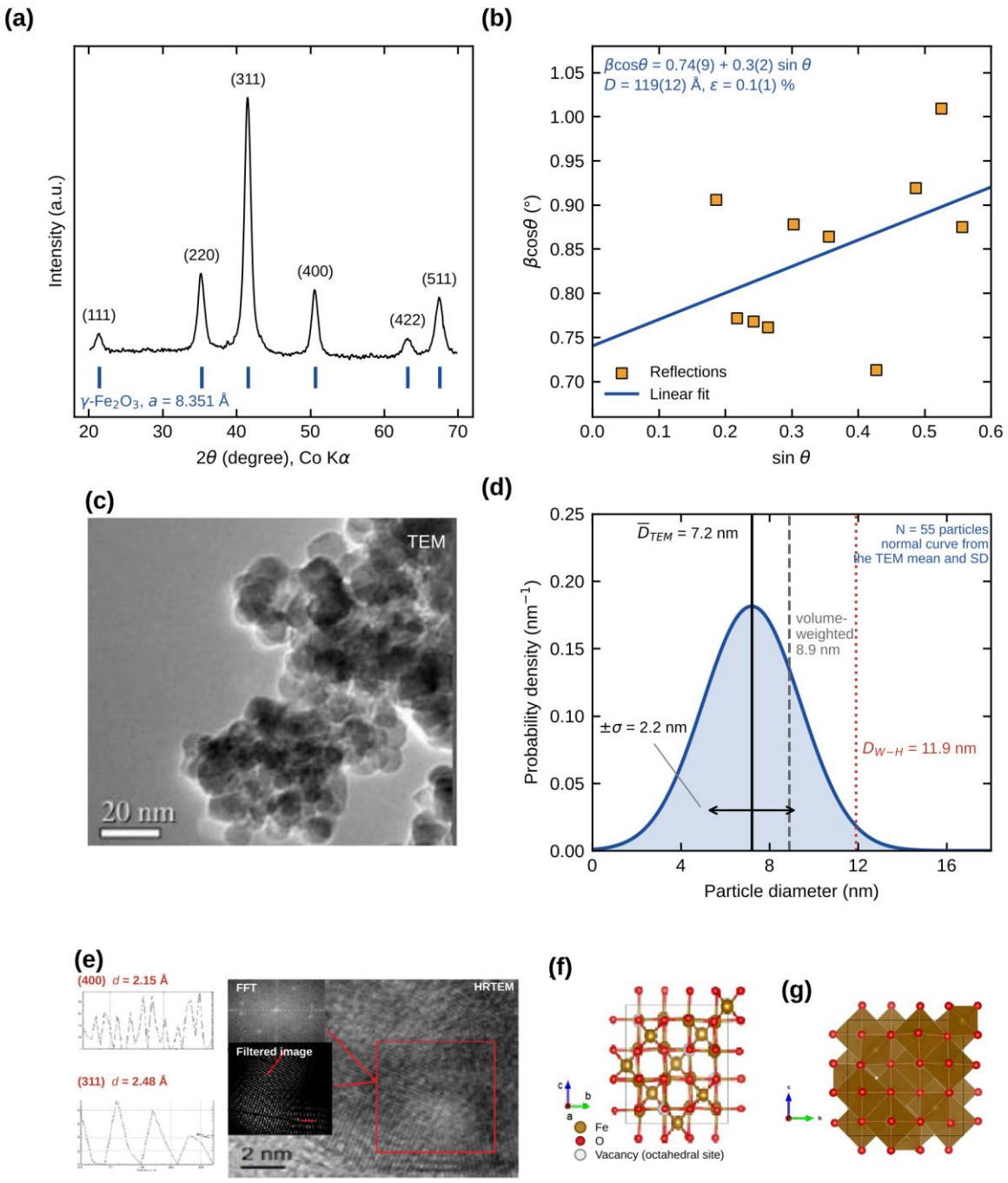


Fig. 3. Structural and morphological characterization of the γ-Fe_2O_3 nanoparticles. (a) XRD pattern (Co Kα); the blue ticks give the positions calculated for maghemite (a = 8.351 Å). (b) Williamson–Hall plot with its linear fit (D = 119 ± 12 Å, ε = 0.1 ± 0.1 %). (c) TEM micrograph showing loosely connected clusters of quasi-spherical particles. (d) Particle-size distribution (N = 55; ⟨D⟩ = 7.2 nm, σ = 2.2 nm) drawn as the normal curve with these parameters; the dashed line is the volume-weighted diameter expected from this distribution (8.9 nm) and the dotted line the W–H crystallite size (11.9 nm). (e) HRTEM image of a single nanoparticle with the corresponding FFT and filtered image; the intensity profiles give lattice spacings of 2.15 Å and 2.48 Å, assigned to the (400) and (311) planes. (f) Unit cell of the spinel structure (Fe: gold; O: red; octahedral vacancies: white sectors). (g) Polyhedral representation of the spinel structure (Fe–O polyhedra: brown; O: red).

The XRD pattern (Fig. 3a) shows six peaks indexed as (111), (220), (311), (400), (422) and (511) of a cubic spinel structure. The peaks are broad (FWHM ≈ 1.0–1.25° in 2θ), which is the signature of coherent diffraction domains of a few nanometers, and the (311) reflection dominates, as expected for spinel ferrites; the relative intensities of the other lines are close to those of a randomly oriented spinel powder, so no marked preferred orientation is expected. The fitted peak positions (2θ ≈ 21.4, 35.3, 41.6, 50.7, 63.2 and 67.5°) coincide within about 0.1° with those calculated for maghemite with a = 8.351 Å (blue ticks in Fig. 3a). The weak superlattice lines (e.g. (210) and (211)) that appear in vacancy-ordered bulk maghemite are not resolved, which suggests that the cation vacancies are distributed at random in these nanoparticles. No additional peak is detected within the sensitivity of the technique, so no secondary phase (such as α-Fe_2O_3) is evidenced. However, the XRD patterns and lattice parameters of maghemite (8.35 Å) and magnetite (8.40 Å) are very close, so that XRD alone cannot distinguish them, and a partial magnetite character (Fe^{2+}) cannot be excluded; this is relevant for the transport properties discussed below. The EDX spectrum (Fig. 2) is in agreement with this phase purity: only Fe and O are detected.

The crystal structure of γ-Fe_2O_3 is shown in Fig. 3f. Maghemite has a cubic spinel-type structure (a ≈ 8.35 Å) in which the O^{2-} anions form a close-packed face-centered cubic sublattice. The Fe^{3+} cations occupy the tetrahedral (A) and octahedral (B) interstitial sites, and the charge balance is ensured by vacancies on the octahedral sublattice, $Fe_{8/3}\square_{1/3}O_4$ (□ = vacancy), so that maghemite can be regarded as a cation-deficient magnetite. In magnetite the octahedral sites are shared by Fe^{2+} and Fe^{3+} ions; any residual Fe^{2+} in the nanoparticles (see below) therefore provides the Fe^{2+}/Fe^{3+} pairs between which small polarons can hop, while the vacancies disorder the octahedral sublattice. In Fig. 3f the octahedral vacancies appear as partially occupied sites. Because all the iron ions of ideal γ-Fe_2O_3 are Fe^{3+}, no electron can hop between equivalent cations and the ideal compound is an insulator; conduction requires a small amount of Fe^{2+}, created for instance by oxygen loss at the surface or by lattice defects. The shortest distance between two octahedral sites, $a\sqrt{2}/4 \approx 2.96$ Å, is then the elementary hopping length of the polarons discussed below.

Fig. 3b shows the Williamson–Hall (W–H) plot, which allows the crystallite size and the microstrain to be separated. The breadth of the observed line is found by the addition of the β_{strain} and β_D, after subtracting the instrumental broadening [10,11].

$$\beta_{hkl} = \beta_{\text{strain}} + \beta_D = 4\varepsilon \tan\theta + \frac{K\lambda}{D\cos\theta}$$

$$\beta_{hkl} \cos\theta = 4\varepsilon \sin\theta + \frac{K\lambda}{D} \quad (1)$$

where λ = 1.78901 Å, K represents a constant with an approximate value of 0.9, and β (rad) denotes the peak width. β_{hkl} is the full width at half-maximum (FWHM) corrected for the instrumental broadening. The preceding equation (1) corresponds to the Williamson–Hall equations. This equation resembles the standard linear equation, y = mx + c. Plotting $\beta_{hkl}\cos\theta$ on the y-axis versus 4sinθ on the x-axis gives the W–H plot of γ-Fe_2O_3, shown in Fig. 3b [10]. Through the application of linear regression to the data, the crystallite size has been deduced from the y-intercept, yielding D ≈ 11.9 nm (119 Å), while the strain has been derived from the slope of the linear representation, resulting in a microstrain ε ≈ 0.1 %. In the context of crystalline materials, the density of dislocation lines per unit volume is referred to as dislocation density (δ) according to the definitions provided by Williamson and Smallman [10,12]. The dislocation density was then estimated with the Williamson–Smallman relation $\delta = 1/D^2$.

The points of the W–H plot (Fig. 3b) scatter widely around the straight line and its slope (0.3 ± 0.2°) is not significantly different from zero: the microstrain (ε ≈ 0.1 ± 0.1 %) is therefore negligible, and the broadening of the lines is dominated by the finite size of the coherent domains. For the same reason the dislocation density, $\delta = 1/D^2 \approx 7 \times 10^{15}$ lines m^{-2}, is a size-related estimate and not evidence of a high defect content. Because of the scatter, the intercept, and hence D, is poorly constrained, and 11.9 nm should be regarded as an upper estimate: the Scherrer formula applied to the six resolved peaks of Fig. 3a gives 9–10 nm (instrumental broadening neglected), in better agreement with the volume-weighted TEM diameter (≈ 9 nm, Fig. 3d).

The HRTEM image of a single nanoparticle (Fig. 3e) shows well-defined lattice fringes inside the region highlighted by the red square, which confirms the crystalline character of the particle. The intensity profiles taken along two directions of the image give interplanar spacings of 2.48 Å and 2.15 Å, which are close to the d-spacings of the (311) and (400) planes of cubic maghemite (≈ 2.52 Å and ≈ 2.08 Å, respectively). The FFT of the image (inset at the top center) displays discrete spots rather than rings, which is typical of a single-crystalline nanoparticle. Together with the XRD results, the HRTEM analysis confirms the good crystallinity and the maghemite (γ) structure of the nanoparticles. The measured spacings differ from the bulk values by about −2 % for (311) and +3 % for (400); this is within the usual accuracy of spacings measured on a single image of moderate magnification

(calibration, defocus, pixel size) and does not by itself indicate a lattice distortion. It must also be noted that the (311) and (400) spacings of magnetite (2.53 and 2.10 Å) are almost identical to those of maghemite, so that HRTEM, like XRD, cannot discriminate between the two phases.

The TEM images (Fig. 3c) show that the nanoparticles have a fine, quasi-spherical shape and a relatively narrow size distribution; they are grouped in loosely connected clusters, as expected for an aerogel network, and the particle–particle contacts of this network play a role in the electrical transport discussed below. The nanocrystals show different contrasts, which result from their different crystallographic orientations with respect to the incident electron beam. To identify the phase, the interplanar distance d and the lattice parameter a were calculated:

$$2d_{hkl}\sin\theta = n\lambda \quad \text{and} \quad a = d_{hkl}\sqrt{h^2+k^2+l^2} \tag{2}$$

where, "a" is represented as the lattice constant and the integers h, k and l are Miller indices of diffraction planes. The lattice parameter obtained is a = 8.36 ± 0.01 Å (mean of the six reflections; individual values 8.351–8.366 Å), i.e. very close to maghemite (8.35 Å) and slightly below magnetite (8.40 Å). A linear (Vegard-type) interpolation between the two phases gives a magnetite-like fraction of about 20 %, which corresponds to only ≈ 7 % of the iron atoms being Fe^{2+} (one third of the iron of Fe_3O_4). However, the offset from the maghemite value (0.01 Å) is equal to the uncertainty of the determination, so that this estimate is 20 ± 20 % (0–14 % of Fe^{2+}), and size and surface effects also shift the lattice parameter of nanoparticles. The lattice parameter is therefore compatible with maghemite and does not by itself prove the presence of Fe^{2+}; the Fe^{2+} content is therefore not quantified. A content of a few percent would nevertheless be sufficient to provide the Fe^{2+}/Fe^{3+} pairs needed for polaron hopping.

Raman spectroscopy distinguishes maghemite from magnetite more reliably than XRD, because the vibrational modes of the two spinels differ even though their diffraction patterns are nearly identical. Maghemite, whose spinel structure contains cation vacancies, shows three broad bands near 350 cm^{-1} (T_{1g}), 500 cm^{-1} (E_g) and 700 cm^{-1} (A_{1g}), together with a broad magnon band near 1400 cm^{-1}. Magnetite, in contrast, gives a single strong A_{1g} band at ≈ 670 cm^{-1}, and hematite gives narrow bands at ≈ 225 and ≈ 290 cm^{-1}. The Raman spectrum of the present γ-Fe_2O_3 nanoparticles, recorded between ≈ 20 and ≈ 725 cm^{-1}, is shown in Fig. 4.

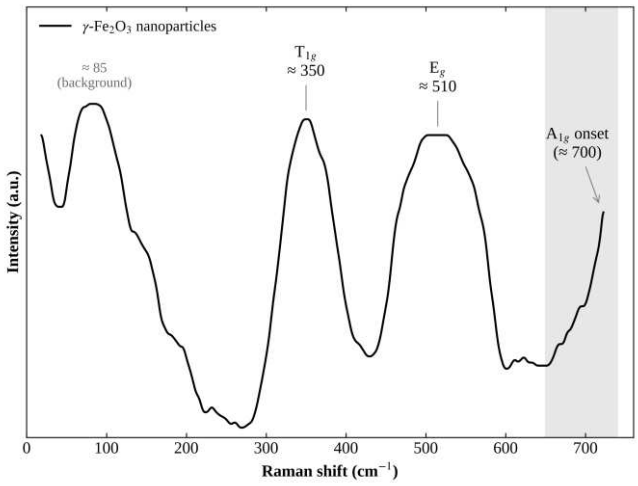


Fig. 4. Raman spectrum of the γ-Fe_2O_3 nanoparticles.

The spectrum of Fig. 4 can be interpreted as follows. Two broad bands are clearly resolved, with maxima at ≈ 350 and ≈ 510 cm^{-1}; the second one is flat-topped and extends from ≈ 490 to ≈ 540 cm^{-1}. They correspond to the T_{1g} and E_g phonon modes of the spinel lattice of maghemite. Above ≈ 650 cm^{-1} the intensity rises steadily up to the end of the recorded range (≈ 725 cm^{-1}): this is the onset of the A_{1g} band (symmetric stretching of the Fe–O bonds of the tetrahedral sites) expected near 700 cm^{-1}, whose maximum lies beyond the recorded range and is therefore not resolved. The intensity is minimal between ≈ 600 and ≈ 650 cm^{-1}: no distinct maximum is observed at ≈ 670 cm^{-1}, where the A_{1g} band of magnetite would appear, and no narrow band is seen at ≈ 225 or ≈ 290 cm^{-1}, which excludes a detectable contribution of hematite (α-Fe_2O_3) and suggests that the laser did not transform the sample during the acquisition. The additional intensity below ≈ 150 cm^{-1}, with a maximum near 85 cm^{-1}, is not assigned to a spinel mode, since this low-wavenumber region is affected by the Rayleigh wing and the instrumental background. The bands are broad and partly overlap because the cation vacancies break the translational symmetry of the spinel lattice and because the crystallites are only a few nanometers in size, which relaxes the Raman selection rules; this is consistent with the broad XRD peaks and with the random distribution of vacancies deduced above. Taken together, the positions of the T_{1g} and E_g bands, the onset of the A_{1g} band above 650 cm^{-1} and the absence of hematite bands support the maghemite character found by XRD (a = 8.36 Å) and a composition close to that of Fe^{3+}-only maghemite, in line with the insulating behavior at low temperature and the megaohm grain-boundary resistance discussed below. A small Fe^{2+} content, which would add a shoulder near 670 cm^{-1}, cannot be excluded because the A_{1g} region is only partly covered.

The crystallite size derived from the XRD results (≈ 12 nm, volume-weighted) is larger than the mean particle size observed by TEM (≈ 7 nm, number-weighted, Fig. 3d), as expected because the volume-weighted average is dominated by the largest particles of the distribution; both methods point to nanoparticles of about ten nanometers. These results provide the structural basis for the analysis of the electrical properties presented below. Since the volume-weighted TEM diameter is ≈ 9 nm and the Scherrer sizes of the individual peaks are 9–10 nm, the W–H value is probably an upper bound; within this uncertainty the coherent diffraction domain coincides with the particle, i.e. the nanoparticles are essentially single crystals, in line with the HRTEM observation. The electrical properties are therefore expected to be governed by the contacts between particles rather than by internal grain boundaries.

The size of the nanoparticles (≈ 12 nm) is below the typical single-domain size of iron oxides, so that superparamagnetic behavior is expected at room temperature [4]. The magnetic susceptibility is discussed at the end of this section.

Fig. 5 shows the ac conductivity spectra of the maghemite nanoparticles at different temperatures. Two regimes are observed. Below about 420 K the conductivity is dispersive: it is nearly flat or slightly decreasing at low frequency, passes through a shallow minimum around 10 kHz and then increases with frequency following a power law. Above 440 K the spectra are completely flat over the whole frequency window, i.e. the conductivity is equal to its dc value, which increases from about 1 µS at 440 K to about 200 µS at 600 K. The dispersive part is described by a power law. The ac conductivity was analyzed with Jonscher's power law [13–16]:

$$\sigma(\omega, T) = \sigma_{\mathrm{dc}} + A(T)\omega^{s(\omega,T)} \qquad (3)$$

where σ_{dc} is the dc conductivity, A is a pre-exponential factor and s ($0 < s \leq 1$) is the frequency exponent (taken as constant at a given temperature; the local exponent d ln σ / d ln ω plotted in Fig. 6 is a different, derived quantity).

The ac conductivity spectra of maghemite nanoparticles display typical semiconducting behavior, with conductivity increasing with both frequency and temperature. This is consistent with a hopping conduction mechanism, which is common in nanostructured and disordered materials [14,17].

The low-frequency plateau of Fig. 5 corresponds to the dc conductivity, and the power-law increase at higher frequency is the usual signature of the hopping of localized carriers (universal dynamic response). The slight decrease of σ below 10 kHz at low temperature is probably due to interfacial polarization (grain boundaries, contacts) rather than to bulk

hopping. As the temperature rises, the plateau rises and the frequency at which the dispersion sets in increases with σ_{dc}; above 440 K it lies beyond the highest measured frequency, so that the spectra appear flat. The flat spectra therefore do not mean that hopping has stopped but that the hopping rate is then faster than the measurement window. Overall, σ increases by about four orders of magnitude between 300 and 600 K, with a steeper rise (a factor of about 7) between 420 and 440 K that is examined below. This strong, thermally activated variation of the conductivity over a wide temperature range, with a single activation energy above 440 K, is the behavior sought for negative-temperature-coefficient (NTC) thermistor-type temperature sensors.

Fig. 6 shows the local frequency exponent s, defined as the logarithmic slope of the conductivity spectra, at various temperatures. Between 300 and 380 K, s rises steeply at low frequency, passes through a broad maximum (0.4–0.65) between about 15 and 100 kHz and then decreases at higher frequency, while for T ≥ 440 K it remains close to zero over the whole range, which reflects the dc plateau. The values of s are always well below unity. The temperature dependence of the exponent obtained by fitting the spectra with Eq. (3) is shown in Fig. 7 and discussed below. The fact that s remains below 1 at all frequencies indicates hopping between localized states rather than a purely capacitive response (s = 1). The maximum of s(ω) moves toward higher frequency as the temperature increases (≈ 15 kHz at 300 K, ≈ 70–80 kHz between 340 and 380 K), in line with the thermal activation of the hopping rate.

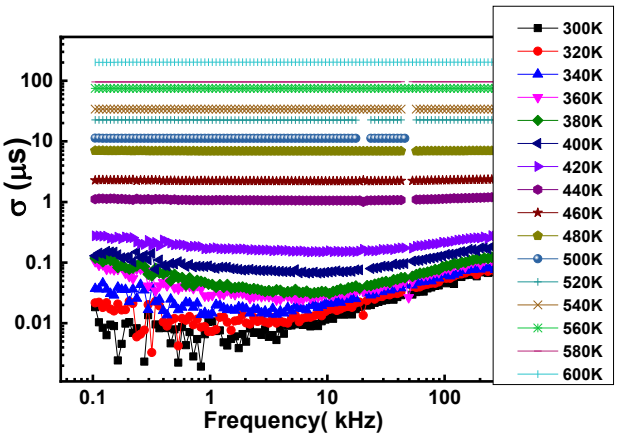


Fig. 5. ac conductivity spectra at different temperature of the maghemite nanoparticles.

To identify the conduction mechanism, the behavior of the exponent s is compared with the predictions of the models usually considered for hopping conduction: quantum mechanical tunneling (QMT), overlapping large-polaron tunneling (OLPT), non-overlapping small-

polaron tunneling (NSPT) and correlated barrier hopping (CBH) [14,17–21]. In the QMT framework, electrons move between lattice sites with a well-defined vibrational phase coherence, whereas CBH describes thermally activated, incoherent hopping over a barrier. In the CBH model s decreases with increasing temperature; in the NSPT model s increases with temperature; in the OLPT model s first decreases, goes through a minimum and then increases. As shown in Fig. 7, the fitted exponent of the Fe_2O_3 nanoparticles is not monotonic: it decreases from 0.56 at 300 K to a minimum of 0.44 at 340 K and then increases up to 0.66 at 420 K, so it never approaches unity. Above 440 K the exponent of the dispersive term (s_{high}, right axis) falls from 0.02 to ≈ 0.001 and vanishes: the amplitude of the dispersive term becomes negligible, so that s is no longer defined by the fit and these values have no physical meaning other than the disappearance of the dispersion. The decrease of s between 300 and 340 K is compatible with CBH or OLPT (local hopping with a low activation energy), whereas its increase between 340 and 420 K is the signature of NSPT; the minimum is the behavior expected for OLPT. These qualitative trends suggest that more than one hopping mechanism of polarons between Fe^{2+} and Fe^{3+} ions may operate in the nanoparticles, and that a single CBH mechanism cannot account for the data. Since the trend of s(T) alone cannot discriminate unambiguously between these models, this assignment remains qualitative. It should be stressed that the decrease of s above 400 K does not reflect a CBH mechanism but the progressive emergence of the dc plateau, which overtakes the power-law term; no barrier height is therefore extracted from it.

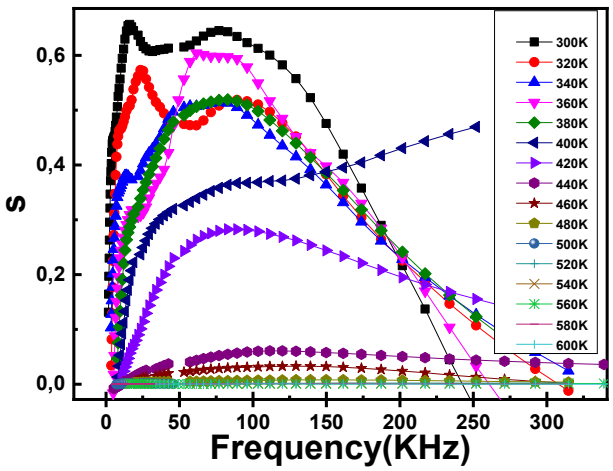


Fig. 6. Local frequency exponent s versus frequency at different temperatures for the maghemite nanoparticles.

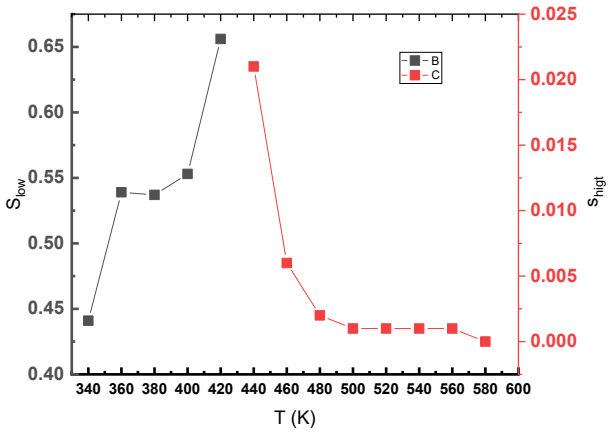


Fig. 7. Variation of the frequency exponent 's' with temperature for maghemite aerogel nanoparticles (s_{low}, left axis, 340–420 K; s_{high}, right axis, 440–580 K).

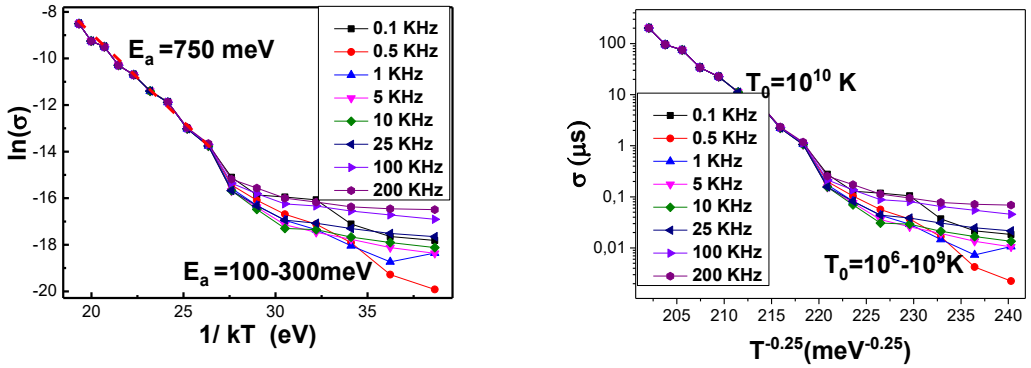


Fig. 8. Variation of the conductivity σ as a function of (a) 1/kT and (b) $T^{-0.25}$ at different frequencies for maghemite aerogel nanoparticles.

Fig. 8a shows ln σ as a function of 1/kT for several frequencies. Above ≈ 440 K the curves superimpose, which confirms the frequency independence of the conductivity, and give a single activation energy E_a ≈ 0.73 eV (≈ 750 meV in Fig. 8a) according to the Arrhenius law $\sigma_{dc} = \sigma_0 \exp(-E_a/k_BT)$. Below ≈ 420 K (1/kT ≈ 27.5 eV^{-1}) the curves split according to frequency and bend toward a much weaker slope, with apparent activation energies of 0.1–0.3 eV (100–300 meV). These low values are similar to those previously reported [18] and correspond to the local hopping of polarons between neighboring Fe^{2+} and Fe^{3+} sites, or inside a grain, which is the process probed by the ac measurement at low temperature. In contrast, the larger value of 0.73 eV characterizes the conduction above 440 K, where the dispersion has disappeared. In a nanoparticle aerogel the current has to cross a large number of particle–particle contacts, which act as additional potential barriers in series with the intragrain hops; the dc activation energy is therefore expected to contain both contributions, which may

explain why it is several times larger than the local one. The quasi-dc resistance extracted from the impedance fits (Table 1) is also thermally activated below 420 K, with an activation energy of about 0.3 eV (315 meV, see below), so that the activation energy of the quasi-dc conduction itself increases from ≈ 0.3 eV to 0.73 eV. In a small-polaron conductor whose carrier density depends on temperature, the dc activation energy is the sum of the hopping barrier and of the energy needed to create or release the carriers, $E_a = E_h + E_g/m$, with m = 1 for a carrier released from a trap and m = 2 or 3 for carriers produced by a defect reaction obeying the mass-action law. Taking $E_h \approx 0.3$ eV from the low-temperature data and $E_a = 0.73$ eV above 440 K gives $E_g \approx 0.4$ eV for m = 1 (polarons released from Fe^{2+}–oxygen-vacancy or Fe^{2+}–surface-defect pairs) and $E_g \approx 0.9$–1.3 eV for m = 2–3 (oxygen loss). Both ranges are physically reasonable: the first is of the order of the binding energy of a polaron to a charged defect, and the second is much smaller than the energy required to remove oxygen from the bulk of an oxide, as expected for the under-coordinated surface oxygen of ≈ 7 nm particles, in which about a quarter of the atoms lie within 0.3 nm of the surface. The increase of E_a from 0.3 to 0.73 eV is therefore interpreted as the passage from an extrinsic regime, in which the carrier density is fixed by the defects frozen in during the synthesis and only the hopping is thermally activated, to a regime in which the carrier density is itself thermally controlled; in the aerogel, the inter-particle contacts, which act as barriers in series with the intragrain hops, are where this thermally released population becomes effective for long-range transport.

Because conduction in disordered and nanostructured oxides is often ascribed to variable-range hopping (VRH), the data were also plotted according to Mott's law, $\sigma \propto \exp[-(T_0/T)^{1/4}]$, in Fig. 8b. A straight line is obtained only in a limited temperature range, and the characteristic temperature at high temperature is $T_0 \approx 10^{10}$ K (10^6–10^9 K at low temperature). Such a value is several orders of magnitude larger than those usually reported for VRH in oxides and would imply a localization length of the order of, or smaller than, the interatomic distance, which contradicts the very assumption of variable-range hopping. Mott's VRH is therefore not the operating mechanism, and the dc transport is better described as thermally activated nearest-neighbor hopping of small polarons.

Existence of small polarons and electrical properties. Several experimental facts support the hopping of small polarons between Fe^{2+} and Fe^{3+} ions in the γ-Fe_2O_3 nanoparticles. (i) The conductivity is thermally activated over the whole temperature range: it increases from ≈ 0.01 μS at 300 K (1–10 kHz) to ≈ 1 μS at 440 K and ≈ 200 μS at 600 K, which is a typical semiconducting behavior in which the carriers are localized and move by thermally assisted jumps. (ii) The exponent s is always smaller than 1 and, between 340 and 420 K, it increases

with temperature, which is the signature of the tunneling of small polarons (NSPT); the preceding decrease and the minimum at 340 K are the OLPT-type behavior. (iii) The local activation energies, 0.1–0.3 eV from the ac data and 315 meV from the impedance analysis, are in the range often reported for small-polaron hopping [22,23] (this criterion alone is not discriminating, and the dc value of 0.73 eV lies outside it), and the small Fe^{2+} content of the nanoparticles (maghemite itself contains only Fe^{3+}) provides the sites between which the polarons jump. (iv) The dc activation energy of 0.73 eV is interpreted above as the sum of the hopping barrier and of the energy of carrier release, and it includes the crossing of the inter-particle contacts; moreover, the relaxation of the electric modulus is also thermally activated (E_d = 949 meV). The electrical data are therefore consistent with small polarons, but cannot prove their existence alone.

Between 420 and 440 K the conductivity increases by a factor of about 7 (at 10 kHz), whereas the Arrhenius law with E_a = 0.73 eV predicts a factor of about 2.5 for the same 20 K step, and the low-temperature law ($E_a \approx 0.3$ eV) only about 1.5 (Figs. 5 and 8a); the step corresponds to an apparent activation energy of ≈ 1.5 eV. The quasi-dc resistance of the impedance fits accelerates in the same way (R drops by a factor of 6 between 400 and 420 K, against about 1.5 expected from 0.3 eV; Table 1). The two indicators place the step in adjacent 20 K intervals (400–420 K for R, 420–440 K for σ at 10 kHz, a comparison that mixes the dispersive and dc contributions), so that the crossover is located between ≈ 400 and 440 K (around 420–430 K) rather than at a sharply defined temperature. This excess coincides with the end of the s_{low} branch and the beginning of the s_{high} branch in Fig. 7, and with the disappearance of the dispersion. Two general remarks guide the interpretation. First, a simple switch between two parallel Arrhenius channels cannot give an apparent activation energy larger than the largest of the two (0.73 eV); an apparent value of ≈ 1.5 eV therefore requires a temperature-dependent prefactor, i.e. a population of carriers (or a number of conducting paths) that increases abruptly with temperature. Second, the γ→α transformation of maghemite nanoparticles is generally observed at much higher temperatures (typically above ≈ 600 K), and the single Arrhenius law with E_a = 0.73 eV followed from 440 to 600 K shows that no further change takes place in this range; the step is therefore not related to a transformation of the iron oxide phase. We tentatively propose that the crossover results from two coupled processes. (i) Thermal release of additional Fe^{2+} carriers: the desorption of strongly bound surface hydroxyl groups and of residual organic species of the synthesis (acetylacetonate and ethoxy groups), which typically takes place in the 400–500 K range, may be accompanied by the loss of surface oxygen, $2Fe^{3+} + O^{2-} \rightarrow 2Fe^{2+} + V_O + ½O_2$, and by the

injection of electrons into the iron sites. This raises the Fe^{2+}/Fe^{3+} ratio, hence the number of hopping pairs, in nanoparticles in which about one quarter of the atoms are at the surface. This reduction is favored in vacuum, in an inert gas or in the presence of reducing organic residues, whereas in air the oxygen would tend to re-oxidize Fe^{2+}; the atmosphere of the impedance measurements, which is not specified in Section 2, is therefore a key parameter. (ii) Activation of the conduction paths through the particle network: the electron exchange between neighboring nanoparticles is controlled by their surface layer, whose Fe^{2+} content and hydroxyl coverage change in the same temperature range, so that the clusters of the aerogel become connected into a continuous conducting network above a threshold temperature; the conductivity then becomes frequency independent and the dispersion leaves the measured window. The loss of adsorbed water and hydroxyl groups also suppresses the contribution of surface protonic conduction (Grotthuss-type hopping, typically 0.1–0.4 eV), which probably participates in the dispersive low-temperature regime and in the polarization below 10 kHz. Other contributions cannot be excluded: the pyrolysis of the organic residues, which may leave conducting carbonaceous bridges between the particles, the necking of the contacts, or the removal of adsorbed water that blocks them.

Origin of the electrical properties. Ideal maghemite contains only Fe^{3+} and is an insulator; the carriers are supplied by Fe^{2+} ions of extrinsic origin. Two sources are consistent with the present data: (a) the reducing medium of the synthesis (supercritical ethanol and the organic ligands of the precursor), which may leave a small magnetite-like (Fe^{2+}-containing) fraction, in agreement with a lattice parameter (8.36 ± 0.01 Å) that cannot be distinguished from, but is marginally above, that of maghemite (8.35 Å); and (b) the oxygen deficiency of the surface of 7 nm particles, where the Fe^{3+} ions are under-coordinated and the oxygen vacancies are compensated by Fe^{2+} ions. The cation vacancies of maghemite do not themselves supply Fe^{2+}, since in the ideal structure their charge is compensated by Fe^{3+}; they act rather on the disorder of the octahedral sublattice (see below). The electron added to an Fe^{3+} site polarizes the surrounding oxygen octahedron, and the resulting small polaron hops between neighboring octahedral sites separated by $a\sqrt{2}/4 \approx 2.96$ Å with a barrier W_H [24]. In the language of electron transfer, the $Fe^{3+} + e^- \rightleftharpoons Fe^{2+}$ self-exchange has a barrier $\lambda/4$, where λ is the reorganization energy of the Fe–O polyhedra [25]; values of λ of the order of 1–1.5 eV, which are expected for iron oxides, give barriers of 0.25–0.4 eV, in line with the 0.1–0.3 eV (ac) and 315 meV (impedance) measured here. The random distribution of the vacancies, deduced from the absence of superlattice lines, produces site-energy disorder, which accounts for the dispersive Jonscher response and for the broad distribution of hopping rates. The EDX

analysis (Fig. 2) points in the same direction as the oxygen deficiency invoked in (a) and (b) (O/Fe ≈ 1.30, against 1.5 for γ-Fe_2O_3), but only qualitatively: a ratio below that of Fe_3O_4 (1.33) is not compatible with the Raman and XRD results, so that the oxygen quantification is clearly biased (absorption of the O Kα line, standardless analysis, residual organic species), and this ratio is not converted into an Fe^{2+} fraction. The Fe^{2+} content is estimated only from the lattice parameter (≈ 7 % of the iron atoms, 0–14 % within the uncertainty)

Origin of the impedance (electrochemical) response. The impedance is that of a network of crystalline particles about 7 nm in diameter joined by small contacts. The charging energy of such a particle in a low-permittivity environment, $e^2/(4\pi\varepsilon_0\varepsilon_m D) \approx 0.2/\varepsilon_m$ eV for D = 7 nm (ε_m: permittivity of the surrounding medium), adds a barrier of the order of 0.1 eV to the transfer of a carrier between neighboring particles [26], and the 30 % spread of the particle size broadens it. The contacts therefore behave as a resistance in parallel with a constant-phase element (Eq. 4): the near-Debye character (α ≈ 1) and the almost temperature-independent capacitance (≈ 10.5–11.4 pF, Table 1), which is that of a bulk-type, geometric response [27], show that the relaxation time τ = RC is controlled by the thermally activated resistance, i.e. by the transfer of carriers across the contacts, in agreement with the equality of the activation energies of R and of τ (≈ 0.37 eV between 300 and 420 K). The slight decrease of σ below 10 kHz at low temperature is the signature of the accumulation of carriers at the contacts and at the electrodes (Maxwell–Wagner–Sillars interfacial polarization), which disappears when the carrier transfer becomes faster than the measuring window.

Maghemite behaves as an insulator at ambient temperature and its conductivity increases strongly with temperature (Figs. 5 and 8a). The electrical conduction in ferrites results from the hopping of electrons (small polarons) between ions of the same element that exist in multiple oxidation states, dispersed randomly over equivalent crystallographic sites [19]. In γ-Fe_2O_3 this is the Fe^{2+}/Fe^{3+} pair, the Fe^{2+} ions being possibly created by the oxygen deficiency of the surface and by lattice defects of the nanoparticles. The γ-phase is metastable and transforms into α-Fe_2O_3 at high temperature, which is generally observed at temperatures higher than those explored here (see below).

The impedance spectra (Fig. 9) were analyzed with the equivalent circuit of Eq. (4). The impedance response of the polycrystalline specimen can be written as:

$$Z = R_g + \frac{R_{\mathrm{bg}}}{1 + RC(j\omega)^{\alpha}} \qquad (4)$$

$0<\alpha<1$ is used to find out the deviation from the ideal Debye response (**α=1**), R_g is the grain resistance and R_{bg} is the boundary grain resistance. α is close to unity at all temperatures

(Table 1), i.e. the relaxation is close to a Debye one. In Eq. (4), C is the coefficient of the constant phase element.

Consequently, a singular combination of parallel resistance (R) and capacitance (C) has been determined to align most closely with the empirical data pertaining to the nanoparticle of Fe_2O_3. The average relaxation time is derived from the relationship $\tau = 1/\omega = (RC)^{1/\alpha}$, where ω is the angular frequency of the maximum of the imaginary part of the impedance. The grain characteristics of the Fe_2O_3 nanoparticle, acquired through the fitting of the empirical data to Equation 4, are given in Table 1. As illustrated in Fig. 9, two distinct semicircles can be identified within the Nyquist plots corresponding to each sample. The semicircles observed in the high-frequency range and the low-frequency range are ascribed to the grain resistance (R_g) and the boundary grain resistance (R_{bg}), respectively. The equivalent circuits are composed of a series resistor (R_g) in conjunction with a parallel arrangement of a resistor (R_{bg}) and a constant phase element capacitor (CPE). In Fig. 9 the arc is fully resolved only at the highest temperatures; at low temperature only its beginning falls within the frequency window, so that the corresponding resistances of Table 1 are obtained by extrapolation of the fit and carry a larger uncertainty. The arcs are centered close to the real axis ($\alpha \approx 1$), i.e. the relaxation is nearly Debye, and the decrease of the arc diameter with temperature reflects the thermally activated decrease of the resistance.

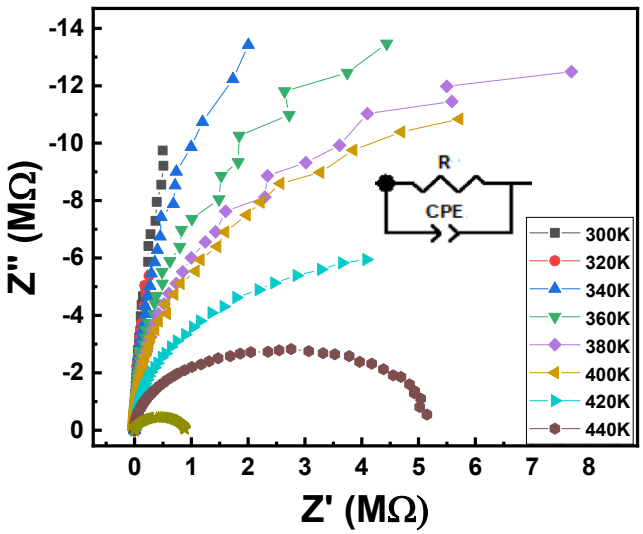


Fig. 9. Nyquist plots of maghemite aerogel nanoparticles at different temperatures. The inset figure show the equivalent circuit.

Table 1
Values of equivalent circuit parameters deduced from experimental data fits

T(K)	R (MΩ)	C(pF)	α
300	102.4	11.07	0.99649
320	50.475	10.5	1
340	32.212	10.45	1
360	29.424	10.52	1
380	13.33	10.82	0.99825
400	5.4411	10.53	1
420	0.89323	11.35	0.99519

The resistance R_{bg} of the grain boundaries obtained is within the megaohm (MΩ) range, which reflects the insulating character of the sample at low temperature. Consequently, impedance spectroscopic analysis of the Fe_2O_3 nanostructure yields grain resistance and the corresponding capacitance in the frequency range of 100 Hz to 1 MHz. It has been observed that both the resistance of the grain interior and the relaxation time diminish with an increase in temperature. Since $\alpha \approx 1$ (Table 1), the relaxation is close to a Debye one, with at most a weak Cole–Cole-type deviation. The activation energy associated with the grain-boundary resistance R_{bg} was determined by fitting the data to the Arrhenius equation [22,23]:

$$R_{\mathrm{bg}} = R_0 \exp\left(-\frac{E_a}{k_{\mathrm{B}}T}\right) \tag{5}$$

An activation energy of 315 meV is obtained from the temperature dependence of R between 300 and 420 K (Fig. 10). It is noteworthy that these measurements are predominantly influenced by the fluctuations in carrier mobility instead of their concentration and are observed to lie between Fe^{3+} and Fe^{2+} ions. Furthermore, the activation energy can be associated with the electrical energy barrier that charge carriers must surmount during the hopping process. The recorded E_a values, which are below 400 meV, are consistent with small-polaron hopping [28–30]. The activation energy depends on the temperature range considered: from the values of Table 1 one finds about 0.27 eV between 300 and 400 K and 0.37 eV when the 420 K point is included, the faster drop of R near 420 K being the first manifestation of the crossover discussed later. The value of 315 meV is therefore representative of the low-temperature regime. In Fig. 10, R_{bg} exceeds R_g by more than four orders of magnitude (MΩ against Ω), so that the dc resistance of the compact is controlled by

the grain boundaries and inter-particle contacts; R_g is defined only between 360 and 440 K and is not monotonic, and should be considered qualitatively.

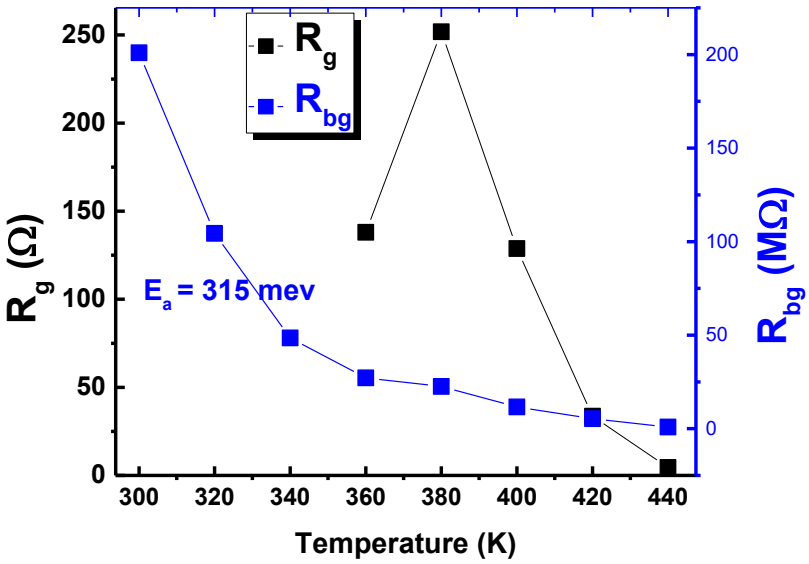


Fig. 10. The evolution of R_g and R_{bg} from fitting of the impedance response for maghemite aerogel nanoparticles.

The phase angle (θ) is given as follows,

$$\theta = \tan^{-1}\left(\frac{Z''}{Z'}\right) \tag{6}$$

Figure 11 illustrates the fluctuation of phase angle (θ) in relation to frequency across different measurement temperatures. In Fig. 11, it is observable that the impedance phase transitions from 0 in a negative direction to −90° as frequency increases from low to high values. The curve converges to two horizontal asymptotes: one at zero for low frequencies and another at −90° for high frequencies. From this data, one can infer that the sample passes from a resistive behavior at low frequency to a capacitive behavior at high frequency. The inflection point, corresponding to a phase of −45°, signifies the frequency of dielectric relaxation. Elevating the temperature during measurement diminishes the range where the sample shows capacitive properties.

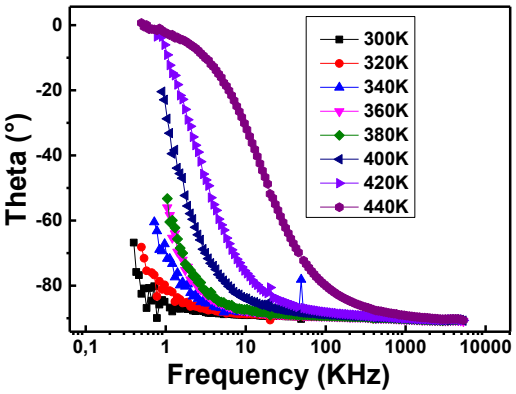


Fig. 11. Variation of phase angle (θ) with frequency at various measurement temperatures.

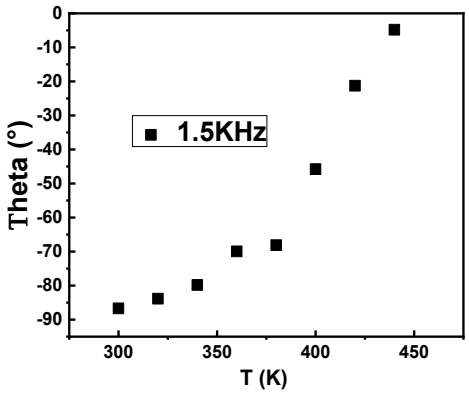


Fig. 12. Evolution of phase of sample impedance versus temperatures at 1.5 kHz.

Figs. 9–11 show that the electrical properties of maghemite aerogel nanoparticles are strongly temperature-dependent: the Nyquist plots show that both the real (Z′) and imaginary (Z″) parts of the impedance decrease as temperature increases from 300 to 440 K, indicating a significant reduction in resistance and enhanced charge transport; this trend is quantitatively confirmed in Fig. 10, where both grain resistance (R_g) and grain boundary resistance (R_{bg}) drop markedly with temperature, consistent with a thermally activated conduction mechanism (activation energy E_a = 315 meV).

Figs. 11 and 12 show that the phase angle shifts to higher frequencies and becomes less negative at elevated temperatures, i.e. the response becomes more resistive (conductive) and the capacitive window shrinks. The phase angle at 1.5 kHz (Fig. 12) increases steadily with temperature, in agreement with the thermally activated conduction. The relaxation frequency, read at θ = −45°, moves from below 1 kHz at 300 K to about 20 kHz at 440 K (Fig. 11), and at 1.5 kHz the phase goes from ≈ −46° at 400 K to ≈ −5° at 440 K (Fig. 12). The sample thus behaves as an insulating dielectric (θ ≈ −90°) up to about 360 K and approaches a resistor (θ → 0) near 440 K, in agreement with the thermal activation of R_{bg} and of the modulus peak.

This insulating, predominantly capacitive behavior at low temperature, with a capacitance almost independent of temperature (≈ 10.5–11.4 pF, Table 1), is of interest for dielectric components operating below ≈ 360 K.

The electric modulus provides valuable insights into the impedance contributions from both the grains and the grain boundaries present in our samples, serving as a tool for understanding the dielectric relaxation mechanism. The complex electric modulus (M*) is defined as follows:

$$M^* = M' + jM'' = \frac{1}{\varepsilon^*} \tag{7}$$

Here, M′ and M″ represent the real and imaginary components of M*, respectively. Fig. 13 presents the electric modulus used to investigate the frequency dependence related to the interfacial polarization effect of maghemite nanoparticles.

Fig. 13 provides additional insight through electric modulus formalism (M″ vs M′), displaying temperature-dependent arcs that shift toward lower M′ values as temperature increases, which indicates changes in the relaxation dynamics and capacitive nature of the maghemite. The variation of the electric modulus (M″vs M′) in maghemite reflects thermally activated relaxation processes [28,29]. As temperature increases, the arcs in M″-M′ plots shift toward lower M′ values, indicating reduced capacitive behavior and altered relaxation dynamics. The decreasing resistance of grain boundaries (R_{bg}) with temperature further supports enhanced ionic or electronic mobility, which modifies the dielectric response captured by the electric modulus formalism. These modifications emphasize the relationship between the microstructure (grains and grain boundaries) and the electrical response in maghemite aerogels subjected to heat.

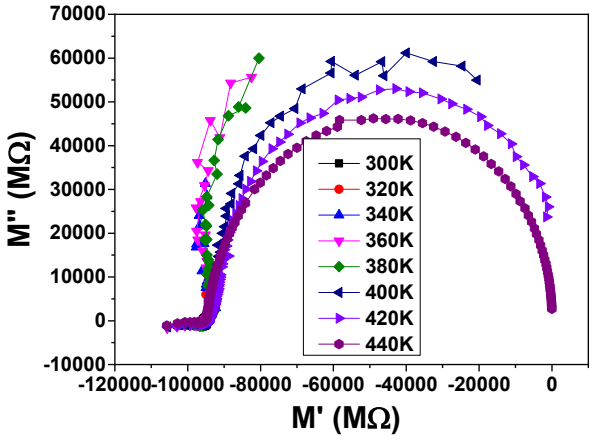


Fig. 13. Imaginary part M″ versus real part M′ of the electric modulus at different temperatures.

Figure 14 illustrates the dependence of the electrical modulus (both real and imaginary components) on frequency. The real component of the modulus exhibits an increasing trend with rising frequency. Conversely, the imaginary component of the electrical modulus remains relatively stable at 460 K. At elevated frequencies, an escalation in M′ and M'' is noted; these observations may be attributed to the absence of restoring forces that govern carrier mobility in response to the applied electric field.

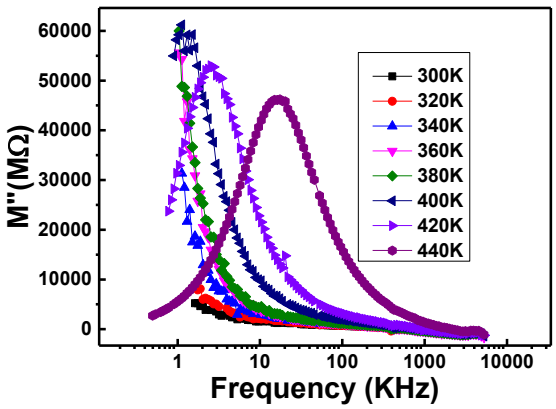


Fig. 14. Variation of real part and imaginary part of electric modulus with frequency

The value of $\omega_{max} = \omega_0$ is taken at the maximum of M″(f) (Fig. 14). Then ω can be written as

$$\omega_0 = \omega_{00} \exp\left(-\frac{E_d}{k_B T}\right) \tag{8}$$

where ω_{00} represents the pre-exponential factor, k_B denotes the Boltzmann constant, and E_d signifies the activation energy pertinent to the relaxation of the electric modulus. The relationship between ω_0 and temperature is depicted in Fig. 15.

An increase of ω_0 with temperature is observed in this analysis. From the slope of the plot of ln ω_0 against $1/k_BT$, the activation energy of the relaxation is E_d = 949 meV (Fig. 15). In a simple hopping picture the relaxation and conduction energies are expected to be close [30–32], since the modulus peak satisfies $\omega_M = \sigma_{dc}/(\varepsilon_0\varepsilon_\infty)$. The larger value of E_d than the dc value (0.73 eV) is explained by the temperature interval of the fit. The three points (400, 420 and 440 K) straddle the conduction crossover, in which the conductivity itself increases with an apparent activation energy of ≈ 1.5 eV; between 400 and 440 K the M″ peak moves from ≈ 1 kHz to ≈ 16 kHz, which corresponds to an apparent energy of ≈ 1.05 eV, and E_d = 0.95 eV lies between the 0.73 eV of the stable high-temperature regime and the 1.5 eV of the step. E_d therefore reflects the same carrier-generation process as the dc conductivity rather than a different relaxation mechanism, and a fit restricted to T ≥ 440 K is expected to converge to

the dc value. The hopping phenomenon is contingent upon the activation energy that corresponds to the electrical energy barrier confronted by the electrons during the hopping process. Given that $\tau = 1/\omega_0 = 1/2P$, where P represents the hopping probability, the observed reduction in relaxation time with temperature leads to an enhancement in the hopping probability with rising temperature [31]. The M″ maximum moves from ≈ 1 kHz at 400 K to ≈ 16 kHz at 440 K, i.e. the relaxation time decreases by more than an order of magnitude over 40 K, and its height decreases slightly, which corresponds to a small increase of the effective capacitance. Since the characteristic frequency of the relaxation moves from ≈ 1 kHz to ≈ 16 kHz between 400 and 440 K, the dielectric response of these nanoparticles is strongly temperature dependent, which could be exploited in temperature-dependent dielectric elements working in the kHz range.

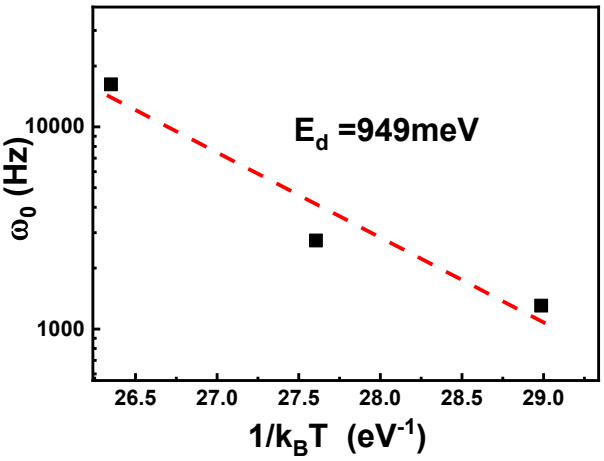


Fig. 15. ω_0 versus $1/k_BT$ for maghemite aerogel nanoparticles.

The relationship between dielectric polarization and electric conduction is intricately linked to the electron transfer between Fe^{2+}/Fe^{3+} ions. In this context, the attenuation of polarization at elevated frequencies is attributed to the inability of electron/hole exchange processes to keep pace with the applied electric field. Comparable findings have been reported previously [32–34]. According to the CBH model, the hopping of charge carriers amplifies with frequency, leading to increased conductivity. At lower frequencies, conductivity is largely influenced by grain boundaries, whereas at higher frequencies, the grains themselves are responsible for the dispersion phenomena [35,36].

These findings enhance the understanding of the electrical properties of nanocrystalline γ-Fe_2O_3 under varying temperature. The intrinsic arrangement of maghemite is based on the inverse spinel structure of Fe_3O_4 (magnetite), with vacancies dispersed throughout the cation sublattice; ideal γ-Fe_2O_3 is therefore anticipated to function as an insulator. However, Serna et al. have shown that nanoparticulate γ-Fe_2O_3 exhibits structural imperfections not solely at the surface but also within the bulk of the particles [36]. These imperfections, the oxygen deficiency of the surface and the Fe^{2+} introduced by the reducing synthesis provide the sites for polaron hopping. In the low-temperature range ($T < 400$ K), the conductivity increases gradually with temperature and its dispersive ac behavior indicates that local hopping within and between neighboring particles dominates, whereas above ≈ 440 K the frequency-independent and more strongly activated conductivity ($E_a \approx 0.73$ eV) indicates long-range transport through the network of nanoparticles, possibly supplied by a thermally increased Fe^{2+} population. Between these two regimes the conductivity rises sharply around 430 K; this crossover is tentatively interpreted as the onset of the thermally activated release of Fe^{2+} carriers (loss of surface hydroxyl groups and oxygen) combined with the activation of the conduction paths between the particles of the aerogel, as discussed above (the contribution of other processes, such as the decomposition of organic residues, is not excluded), and not as a structural transition, since the γ→α transformation is expected at higher temperature and the Arrhenius law is obeyed from 440 to 600 K. The inverse magnetic susceptibility ($1/\chi$) as a function of temperature is displayed in Figure 16: it remains nearly constant up to about 250 K and then increases markedly with temperature. This evolution starts well below the temperature of the conduction crossover (≈ 420–440 K), and the Curie temperature of bulk maghemite lies well above 600 K, so that the magnetic behavior of the particles is not the origin of the anomaly at 430 K.

The plateau of $1/\chi$ below about 250 K and its approximately linear increase above 300 K (Fig. 16) are what is expected for an assembly of superparamagnetic nanoparticles: below the blocking temperature the moments are frozen and the susceptibility is nearly constant, whereas above it the susceptibility follows a Curie-like law. This is consistent with the particle size of about 10 nm and with the room-temperature superparamagnetism mentioned above [4]; the knee near 250–300 K may mark the blocking temperature. Nanoparticles combining a magnetic response of superparamagnetic type with the electrical and dielectric properties described above are of interest for the magnetic and electronic components of the ferrite type mentioned in the Introduction; this was not tested here.

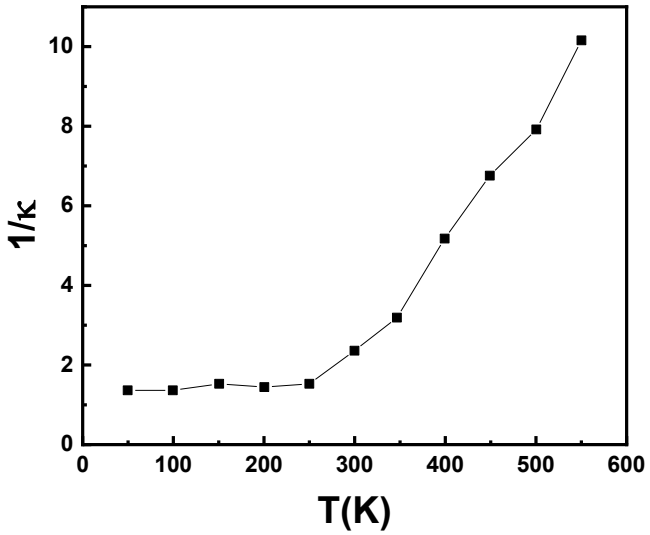


Fig. 16. Plot of the inverse susceptibility as a function of temperature.

The changes in the grain boundary resistance and in the dielectric relaxation dynamics observed by impedance spectroscopy further reflect the enhanced charge transport with temperature. The relationship between nanoscale structure and electrical performance highlights the importance of phase purity, particle size, morphology and, in particular, of the contacts between nanoparticles in the aerogel network, in determining the conduction characteristics of γ-Fe_2O_3 nanoparticles.

The results of this work point to applications that follow directly from the measured electrical and dielectric properties. The strong, thermally activated increase of the conductivity (about four orders of magnitude between 300 and 600 K, with a well-defined activation energy of 0.73 eV above 440 K) is the characteristic of a negative-temperature-coefficient resistive element, so that these nanoparticles are candidates for temperature sensing in the range studied. At lower temperature, the highly resistive and predominantly capacitive response ($R \approx 10^8$ Ω and C ≈ 11 pF at 300 K, phase angle close to −90° up to about 360 K) is that of a dielectric, of interest for dielectric and electronic components, in line with the use of ferrites in electronics mentioned in the Introduction. Above ≈ 420 K the dielectric response changes with temperature (dispersion leaving the measured window, strong decrease of R), which sets the upper working temperature of such a dielectric use.

Potential biomedical applications. Besides the electronic uses above, several properties established in this work are those on which the biomedical use of iron oxide nanoparticles

relies [5,6]. (i) Size and superparamagnetism: the particles are single-crystalline, with a mean TEM diameter of ≈ 7 nm and crystallite sizes of 9–12 nm, i.e. below the single-domain size, and the temperature dependence of $1/\chi$ (Fig. 16) is that of an assembly of superparamagnetic nanoparticles [4]. Such particles carry no remanent moment once the field is removed, which limits their magnetic agglomeration in suspension and is the prerequisite for four main uses: negative (T_2) contrast agents for magnetic resonance imaging, heat generation in an alternating magnetic field (magnetic hyperthermia, in which tumor tissue is heated to about 315–320 K), magnetically guided delivery of drugs, and magnetic separation or labeling of cells and biomolecules. (ii) Phase and chemical stability: Raman and XRD show a maghemite-type spinel without hematite, and maghemite is the oxidized, chemically more stable form of magnetite, which is the reason why γ-Fe_2O_3 is generally preferred to Fe_3O_4 for in-vivo applications. (iii) Synthesis: the sol-gel route with supercritical drying is simple, cost-effective and scalable, and the Gd-doped variants of the same protocol (Section 2) could be explored for dual-modality (T_1/T_2) contrast agents. These applications are suggested by the structural and magnetic results only; the saturation magnetization, the blocking temperature, the specific absorption rate and the relaxivity were not measured here.

The electrical and dielectric results suggest two further, more speculative, biomedical uses. First, the response of the ac conductivity and of the low-frequency polarization to surface hydroxyl groups and adsorbed water (Section 3) shows that the impedance of these nanoparticles is sensitive to their surface state; nanoparticle layers of this type could therefore be tested as the transducer of impedimetric or chemiresistive sensors (for instance humidity or breath monitoring, or the label-free detection of molecules attached to the surface), in line with the use of iron oxides in sensors [18]. Second, between 300 and 320 K the resistance of Table 1 falls from 102.4 to 50.5 MΩ, i.e. by ≈ 3.5 % per kelvin ($E_a \approx 0.3$ eV), a sensitivity of the same order as that of commercial NTC thermistors, while the capacitance stays at ≈ 10.5–11.4 pF and the phase angle close to −90° up to about 360 K. Around the physiological temperature (≈ 310 K) the material is therefore a temperature-sensitive, but electrically stable and predominantly capacitive, dielectric, which could be of interest for small temperature probes or for dielectric elements of biomedical electronic devices. The very high resistance (tens of MΩ), the use of a pellet of powder rather than a film, and the absence of any test in a physiological or aqueous environment must be kept in mind.

Several steps are required before any of these biomedical uses can be considered. The powder obtained here is an aerogel of loosely connected clusters, whereas biomedical applications need stable aqueous colloids of individual, coated particles (for example with dextran, polyethylene glycol, citrate or silica), and the 30 % spread of the particle size must be reduced because the magnetic heating and the relaxivity depend strongly on the size. The residual organic species of the acetylacetonate precursor, mentioned above, must be removed. The oxygen-deficient and partly reduced surface (Fe^{2+}) that supplies the carriers for polaron hopping may also modify the magnetization and the oxidation state of the particles, so that the magnetic and electrical properties must be re-examined after surface coating. Finally, the cytotoxicity, the hemocompatibility and the stability in physiological media were not studied, and the electrical measurements were performed on dry powder between 300 and 600 K, so that the conduction regime above ≈ 420 K has no biomedical relevance.

4. Conclusion

The γ-Fe_2O_3 nanoparticles are single-phase cubic spinel nanoparticles (maghemite-like; crystallite size ≈ 9–12 nm, mean TEM diameter ≈ 7 nm, negligible microstrain ≈ 0.1 %). Their conductivity increases by about four orders of magnitude between 300 and 600 K (≈ 0.01 µS at 300 K, measured at 1–10 kHz, ≈ 1 µS at 440 K and ≈ 200 µS at 600 K). The thermally activated conductivity, the exponent $s < 1$ that increases with temperature between 340 and 420 K, and the low local activation energies (100–300 meV from the ac data; 315 meV from the impedance fits) are consistent with the hopping of small polarons between Fe^{2+} and Fe^{3+} ions, but do not prove it by themselves: the Fe^{2+} content could not be quantified (≈ 7 % of the iron atoms from the lattice parameter, with an uncertainty of the same order, and no Fe^{2+} signature in the partly covered Raman range). The Fe^{2+} carriers are attributed to the reducing synthesis medium and to the under-coordinated, oxygen-deficient surface of the ≈ 7 nm particles, the cation vacancies contributing rather to the site-energy disorder, and the hopping barrier is of the order of λ/4 of the Fe^{2+}/Fe^{3+} electron transfer. Two regimes are identified: a dispersive ac regime below ≈ 420 K, described by Jonscher's power law, and a frequency-independent regime above ≈ 440 K, in which the dispersion has left the measured frequency window. The exponent s is non-monotonic, with a minimum (0.44) near 340 K, which suggests a crossover from CBH/OLPT-type hopping to NSPT rather than a single CBH mechanism, and Mott's variable-range hopping is ruled out ($T_0 \approx 10^{10}$ K). The activation

energy rises from 100–300 meV to 730 meV above 440 K, which corresponds, in the carrier-generation model, to an energy of ≈ 400–1300 meV for the creation or release of the carriers, depending on the mass-action exponent; the long-range conduction above 440 K would then be controlled by thermally released carriers and by the inter-particle contacts. Between ≈ 400 and 440 K the conductivity rises faster than any Arrhenius law (about sevenfold between 420 and 440 K at 10 kHz, against ≈ 2.5 expected for E_a = 730 meV; apparent activation energy ≈ 1500 meV). This step is tentatively attributed to the loss of surface hydroxyl groups and oxygen (possibly with the decomposition of organic residues), which would release Fe^{2+} carriers, and to the activation of the conduction paths of the aerogel network, rather than to a phase transition. The temperature dependence of the inverse susceptibility is consistent with an assembly of superparamagnetic nanoparticles and is not the origin of the conduction crossover.

The structural, magnetic and electrical results point to three groups of uses: temperature sensing and dielectric components in the range studied, and, after surface coating and dispersion in water, biomedical uses of the superparamagnetic nanoparticles (MRI contrast, magnetic hyperthermia, drug targeting, magnetic separation), together with two speculative sensor/thermometry uses of the electrical response. These applications, their prerequisites and their limits are discussed at the end of Section 3; none of the biomedical uses has been tested here.

Funding The authors have not disclosed any funding.

Data Availability The data supporting the findings of this study can be obtained from the corresponding author upon reasonable request.

Declarations

Conflict of interest The authors declare no competing interests.

References

[1] A.K. Boal, in: V.M. Rotello (Ed.), Nanoparticles: Building Blocks for Nanotechnology, Kluwer Academic/Plenum Publishers, New York, 2004.

[2] S. Sun, C.B. Murray, D. Weller, L. Folks, A. Moser, Science 287, 1989 (2000).

[3] S. Sun, Adv. Mater. 18, 393 (2006).

[4] D.K. Kim, W. Voit, W. Zapka, B. Bjelke, M. Muhammed, K.V. Rao, Mater. Res. Soc. Symp. Proc. 676, Y8.32.1 (2001).

[5] P. Majewski, B. Thierry, Crit. Rev. Solid State Mater. Sci. 32, 203 (2007).

[6] M.A. Verges, R. Costo, A.G. Roca, J.F. Marco, G.F. Goya, C.J. Serna, M.P. Morales, J. Phys. D: Appl. Phys. 41, 134003 (2008).

[7] O.M. Lemine, K. Omri, B. Zhang, L. El Mir, M. Sajieddine, A. Alyamani, M. Bououdina, Superlattices Microstruct. 52, 793 (2012).

[8] I. Alotaibi, M.S. Alshammari, S. Algessair, N. Madkhali, N. Abdel All, M. Hjiri, S. Abu Alrub, L. El Mir, O.M. Lemine, Physica B 625, 413510 (2022).

[9] O.M. Lemine, K. Omri, M. Iglesias, V. Velasco, P. Crespo, P. de la Presa, L. El Mir, H. Bouzid, A. Yousif, A. Al-Hajry, J. Alloys Compd. 607, 125 (2014).

[10] B. Biswas, M.L. Rahman, M.F. Ahmed, N. Sharmin, Heliyon 10, e30810 (2024).

[11] G.K. Williamson, W.H. Hall, Acta Metall. 1, 22 (1953).

[12] G.K. Williamson, R.E. Smallman, Philos. Mag. 1, 34 (1956).

[13] S. Somiya, F. Aldinger, N. Claussen, R.M. Spriggs, K. Uchino, K. Koumoto, M. Kaneno, Handbook of Advanced Ceramics, vol. 2, Academic Press, London, 2003, p. 187.

[14] R.D. Gould, A.K. Hassan, Thin Solid Films 223, 334 (1993).

[15] A.K. Jonscher, Nature 267, 673 (1977).

[16] A.K. Jonscher, Dielectric Relaxation in Solids, Chelsea Dielectrics Press, London, 1983.

[17] R. Jana, J. Datta, S. Sil, A. Dey, B. Pal, A. Biswas, P. Ray, Mater. Res. Express 6, 1050d1 (2019).

[18] A.P. Caricato et al., J. Phys. D: Appl. Phys. 40, 4866 (2007); T. Tesfamichael et al., Sens. Actuators B 168, 345 (2012).

[19] I. Zhang, Z. Liu, C. Yang, V. García Sakai, M. Tyagi, Hong, ACS Nano 16, 13771 (2022).

[20] S. Murugavel, M. Upadhyay, J. Indian Inst. Sci. 91, 303 (2011).

[21] S.R. Elliott, Adv. Phys. 36, 135 (1987).

[22] N. Kılınç, L. Arda, S. Öztürk, Z.Z. Öztürk, Cryst. Res. Technol. 45, 529 (2010).

[23] A. Tabib, N. Sdiri, H. Elhouichet, M. Férid, J. Alloys Compd. 622, 687 (2015).
[24] I.G. Austin, N.F. Mott, Adv. Phys. 18, 41 (1969).
[25] R.A. Marcus, N. Sutin, Biochim. Biophys. Acta 811, 265 (1985).
[26] B. Abeles, P. Sheng, M.D. Coutts, Y. Arie, Adv. Phys. 24, 407 (1975).
[27] J.T.S. Irvine, D.C. Sinclair, A.R. West, Adv. Mater. 2, 132 (1990).
[28] M. Benamara, S. Bouzidi, N. Zahmouli, S.S. Teixeira, M.P.F. Graça, L. El Mir, M.A. Valente, Appl. Phys. A 128, 624 (2022).
[29] D. Predoi, C.L. Popa, M.V. Predoi, Polym. Eng. Sci. 57, 485 (2017).
[30] F. Ahmad, A. Maqsood, Mater. Sci. Eng. B 273, 115 (2021).
[31] M.B. Reddy, P.V. Reddy, J. Phys. D: Appl. Phys. 24, 975 (1991).
[32] M.I. Klinger, J. Phys. C: Solid State Phys. 8, 3595 (1975).
[33] D. Ravinder, K. Latha, J. Appl. Phys. 75, 6118 (1994).
[34] P.P. Hankare, R.P. Patil, U.B. Sankpal, S.D. Jadhav, I.S. Mulla, K.M. Jadhav, B.K. Chougule, J. Magn. Magn. Mater. 321, 3270 (2009).
[35] E. Veena Gopalan, K.A. Malini, S. Saravanan, D. Sakthi Kumar, Y. Yoshida, M.R. Anantharaman, J. Phys. D: Appl. Phys. 41, 185005 (2008).
[36] C.J. Serna, F. Bødker, S. Mørup, M.P. Morales, F. Sandiumenge, S. Veintemillas-Verdaguer, Solid State Commun. 118, 437 (2001).